ADVANCED MATERIALS
www.advmat.de

Robust Interface Ru Centers for High-Performance Acidic Oxygen Evolution

*Xiaoju Cui, Pengju Ren, Chao Ma, Jia Zhao, Ruixue Chen, Shiming Chen, N. Pethan Rajan, Haobo Li, Liang Yu, Zhongqun Tian, and Dehui Deng**

RuO_2 is considered as the state-of-the-art electrocatalyst for the oxygen evolution reaction (OER) in acidic media. However, its practical application is largely hindered by both the high reaction overpotential and severe electrochemical corrosion of the active centers. To overcome these limitations, innovative design strategies are necessary, which remains a great challenge. Herein, robust interface Ru centers between RuO_2 and graphene, via a controllable oxidation of graphene encapsulating Ru nanoparticles, are presented to efficiently enhance both the activity and stability of the acidic OER. Through precisely controlling the reaction interface, a much lower OER overpotential of only 227 mV at 10 mA cm^{-2} in acidic electrolyte, compared with that of 290 mV for commercial RuO_2, but a significantly higher durability than the commercial RuO_2, are achieved. Density functional theory (DFT) calculations reveal that the interface Ru centers between the RuO_2 and the graphene can break the classic scaling relationships between the free energies of HOO* and HO* to reduce the limiting potential, rendering an enhancement in the intrinsic OER activity and the resistance to over-oxidation and corrosion for RuO_2.

Electrochemical water splitting in acidic electrolyte has been widely considered as a sustainable and environmentally friendly approach for the production of clean hydrogen fuel.[1–4] However, the oxygen evolution reaction (OER) as the key and bottleneck-type reaction largely hinders the overall efficiency due to its sluggish reaction kinetics,[5–7] in which RuO_2 is considered as the state-of-the-art OER electrocatalyst in acidic media.[8–11] However, the accompanying over-oxidation of RuO_2 to dissolvable RuO_4 at applied OER potentials together with the acidic environment make RuO_2 suffer from strong corrosion and therefore unable to sustain the OER, which seriously prevents its application in acidic electrolyte.[12–17] Although much efforts have been devoted to enhancing the OER performance in acidic electrolyte by the doping of RuO_2 with transition metals or stabilizing RuO_2 with IrO_2,[18–26] it is still a great challenge to concurrently achieve highly active and long-term stable catalysts up to date.

In this study, we report the robust interface Ru centers between RuO_2 and graphene via a controllable oxidation of graphene encapsulating Ru nanoparticles, exhibiting prominently enhanced activity and stability for the acidic OER. Through precisely controlling the reaction interface, we achieve a much lower OER overpotential of only 227 mV at 10 mA cm^{-2} without *i*R-correction in acidic electrolyte, significantly better than the commercial RuO_2 benchmark (290 mV) and outperforming most of the documented electrocatalysts including RuO_2-based and IrO_2-based materials. More importantly, this catalyst offers far better durability than the commercial RuO_2 in 0.5 M H_2SO_4 electrolyte. Density functional theory calculations reveal that the interface Ru centers between RuO_2 and graphene can break the classic scaling relationships between the free energies of HOO* and HO* to reduce the limiting potential. The electron-rich interface could also act as an electron reservoir to donate electrons to the RuO_2 surface and thus help prevent the over-oxidation and corrosion for RuO_2.

The robust interface Ru centers between RuO_2 and graphene was constructed via a controllable oxidation of graphene encapsulating Ru nanoparticles. Considering the graphene shell formed on the Ru nanoparticles is difficult due to its poor carbon deposition ability, we introduced Ni precursors to form the RuNi alloy to facilitate in-situ growing graphene shells encapsulating the Ru nanoparticles. As shown in **Figure 1**a, the precursors of Ru and Ni were first filled into the channel of

Dr. X. Cui, R. Chen, Prof. Z. Tian, Prof. D. Deng
Collaborative Innovation Center of Chemistry for Energy Materials
College of Chemistry and Chemical Engineering
Xiamen University
Xiamen 361005, China
E-mail: dhdeng@dicp.ac.cn
Dr. X. Cui, J. Zhao, R. Chen, Dr. S. Chen, Dr. N. P. Rajan, Dr. H. Li, Dr. L. Yu, Prof. D. Deng
State Key Laboratory of Catalysis
Collaborative Innovation Center of Chemistry for Energy Materials
Dalian Institute of Chemical Physics
Chinese Academy of Sciences
Dalian 116023, China
Dr. P. Ren
State Key Laboratory of Coal Conversion
Institute of Coal Chemistry
Chinese Academy of Sciences
Taiyuan 030001, China
Prof. C. Ma
Center for High Resolution Electron Microscopy
College of Materials Science and Engineering
Hunan University
Changsha 410082, China
The ORCID identification number(s) for the author(s) of this article can be found under https://doi.org/10.1002/adma.201908126.

DOI: 10.1002/adma.201908126

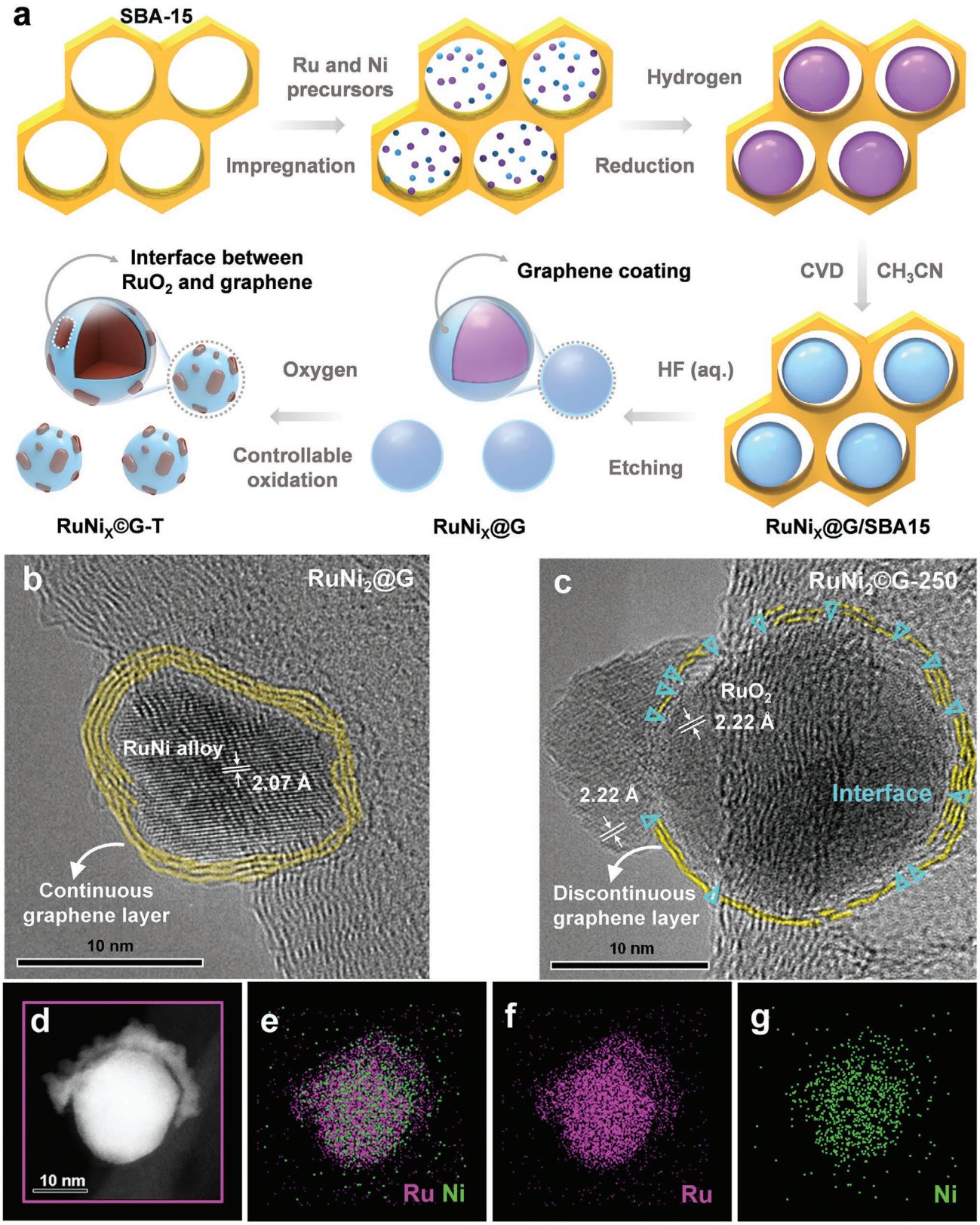

Figure 1. Schematic synthesis process, morphology, and structural characterizations of $RuNi_2$©G-250 and $RuNi_2$@G. a) Schematic illustration of the preparation process for $RuNi_2$©G-250 with interface between RuO_2 and graphene, The symbol "T" represents the different oxidation temperatures, and the symbol "X" represents the molar ratio of Ru and Ni precursors. b) HRTEM image of $RuNi_2$@G. c) HRTEM image of $RuNi_2$©G-250 with unique interface between RuO_2 and graphene. d–g) HAADF-STEM image and the corresponding energy-dispersive spectroscopy maps of $RuNi_2$©G-250 for Ru, Ni, and the combined image.

SBA-15 by an impregnation method. Subsequently, the sample was heated under H_2 atmosphere to form the RuNi alloy nanoparticles, followed by a chemical vapor deposition process to produce graphene shells coating on the RuNi nanoparticles. Then, etching of SBA-15 and bare metals by hydrofluoric acid solution to obtain graphene encapsulating RuNi nanoparticles ($RuNi_X$@G). Further, a controllable oxidation of graphene encapsulating RuNi nanoparticles under different temperatures was adopted to construct highly active interface Ru centers between RuO_2 and graphene, and the catalysts were denoted as $RuNi_X$©G-T (The symbol "T" represents the different oxidation temperatures ranging from 200 to 500 °C, and the symbol "X" represents the molar ratio of Ru and Ni precursors ranging from 1/44 to 2).

The structure of interface between RuO_2 and graphene ($RuNi_2$©G-T) via a controllable oxidation of $RuNi_2$@G under different temperatures was characterized by high-resolution transmission electron microscopy (HRTEM) image, X-ray absorption near-edge structure (XANES), X-ray diffraction (XRD), X-ray photoelectron spectroscopy (XPS), and Raman spectrum. As shown in Figure 1b and Figure S1 (Supporting Information), the synthesized graphene encapsulating RuNi nanoparticles ($RuNi_2$@G) with an average diameter of 5–10 nm was composed of a few layers of graphene shell and the RuNi alloy, which was evidenced by the XRD patterns in Figure S2 (Supporting Information). After a controllable oxidation treatment on $RuNi_2$@G at 200 °C for 1 h, the structure of Ru almost has no change and the chemical state is similar to Ru foil (**Figure 2**a). Once elevating the oxidation temperature to 225 °C, the inner core nanoparticles were gradually oxidized to RuO_2, which implies that graphene shell has been broken and unable to protect the inner nanoparticles from oxidation. Interestingly, the efficient interface between RuO_2 and graphene ($RuNi_2$©G-250) for OER reaction can be achieved by precisely controlling the oxidation temperature at 250 °C as shown in Figure 1c and Figure S3 (Supporting Information), which is identified by high-angle annular dark-field scanning transmission electron microscopy (HAADF-STEM) image with the corresponding elemental mappings (Figure 1d–g). The images illustrate that the interface between RuO_2 and graphene were formed by the over spilling of RuO_2 nanoparticles through ruptured graphene shells. Further increase of the oxidation temperature to 500 °C, the graphene shells gradually disappeared and the corresponding nanoparticles were completely oxidized to RuO_2 finally (**Figure 2**a–c). This is further confirmed by the in-situ XRD characterization showing that the increase of RuO_2 intensity is along with the decrease of graphene and RuNi alloy intensity with the increase of oxidation temperature (Figure 2b). In addition, the CO_2 signal from the temperature programmed oxidation test in Figure S4 (Supporting Information) indicates that the graphene shell can be

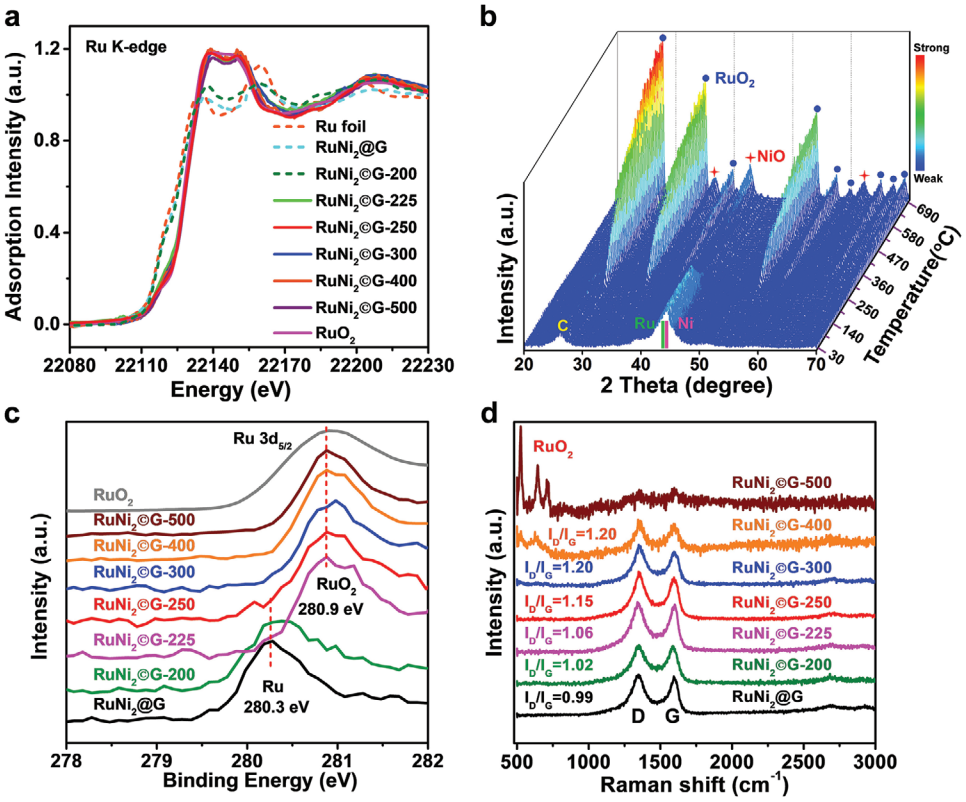

Figure 2. Structural and electronic characterizations of $RuNi_2$@G sample with treatment at different oxidation temperatures. a) XANES of Ru K-edge spectra of $RuNi_2$@G sample treated by different oxidation temperatures. b) In situ high-temperature XRD patterns of $RuNi_2$@G through a temperature-programmed oxidation process by air with a heating rate of 2 °C min^{-1} from 30 to 700 °C and a collecting spectrum rate of 10° min^{-1} from 20° to 70°. c) XPS of Ru 3d spectra of $RuNi_2$@G sample treated by different oxidation temperatures in comparison with commercial RuO_2, the peaks located at the binding energies of 280.3 and 280.9 eV were corresponding to Ru and RuO_2 species.[24,32,33] d) Raman spectra and the corresponding intensity ratio of D peak and G peak (I_D/I_G) for $RuNi_2$@G sample treated by different oxidation temperatures.

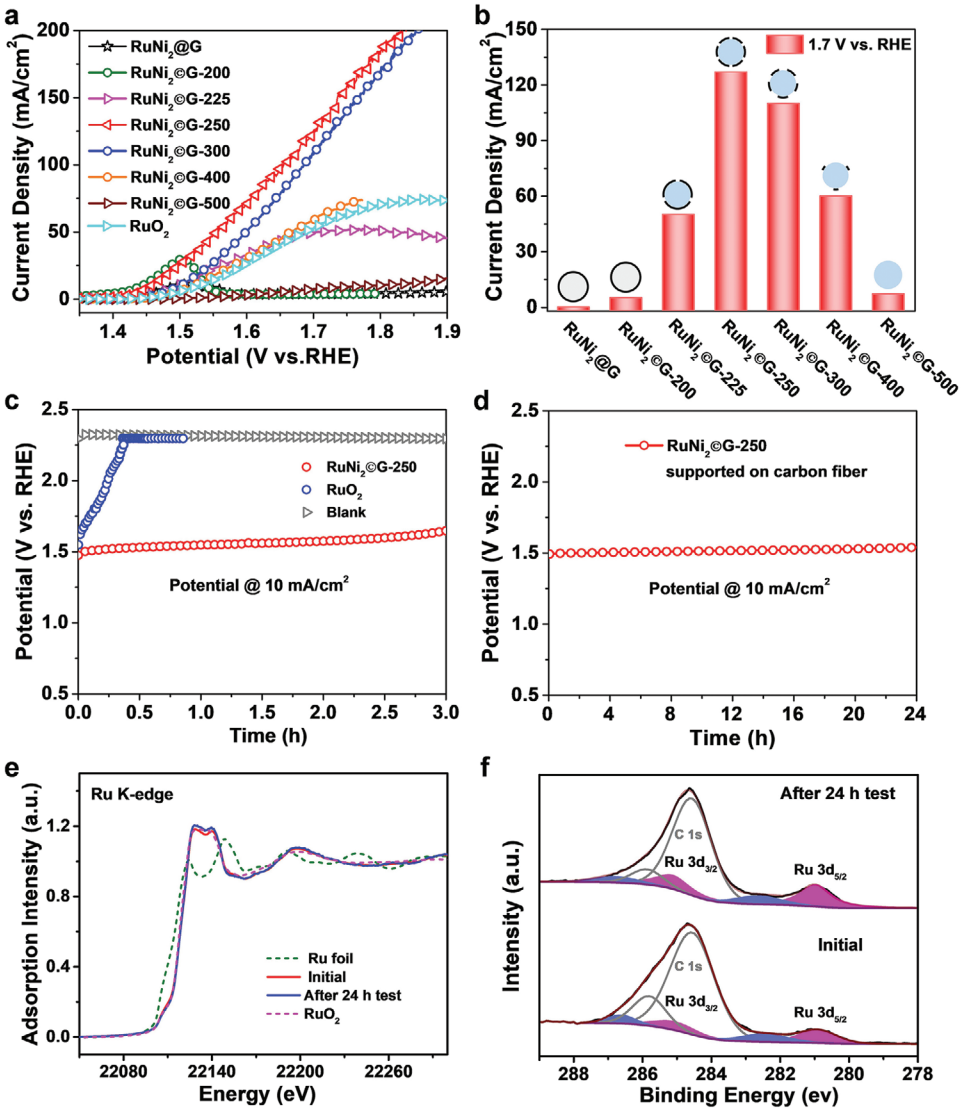

Figure 3. Electrocatalytic OER performance test in O_2-saturated 0.5 M H_2SO_4 solution at 25 °C without *iR* correction and characterizations of $RuNi_2$©G-250 before and after durability testing. a) LSV curves of $RuNi_2$©G-250 in comparison with samples treated at different oxidation temperatures and commercial RuO_2 at the same mass loading of 0.32 mg cm^{-2}. b) The current densities at 1.7 V versus RHE of $RuNi_2$©G-250 in comparison with the $RuNi_2$@G sample treated by different oxidation temperatures; the insert is the schematic diagram of $RuNi_2$@G sample treated by different oxidation temperatures. c) Chronopotentiometric curves for the $RuNi_2$©G-250 and commercial RuO_2 at a current density of 10 mA cm^{-2} at the same mass loading of 0.32 mg cm^{-2} supported on glassy carbon. d) Chronopotentiometric curve obtained with $RuNi_2$©G-250 supported on carbon fiber at a mass loading of 3 mg cm^{-2}. e–f) XANES of Ru K-edge and XPS spectra for $RuNi_2$©G-250 supported on carbon fiber before and after 24 h stability testing.

destroyed only when the oxidation temperature exceeds 200 °C. The Raman spectra show two characteristic peaks of D band (1350 cm^{-1}) and G band (1600 cm^{-1}) in Figure 2d. The corresponding intensity ratio (I_D/I_G) to characterize the concentration of defects show that with the increase of oxidation temperature, the magnitude of I_D/I_G also increased, indicating an increase of the concentration of defects in the graphene layer. These characterizations indicate the formation of interface between RuO_2 and graphene through a controllable oxidation of $RuNi_2$@G at 250 °C, suggesting that the lower or higher oxidation temperatures go against the formation of efficient interface. Hence, via changing the oxidation temperature, we can effectively control the interface between RuO_2 and graphene.

A typical three-electrode electrochemical cell was adopted to evaluate the OER performance of these $RuNi_X$©G-T catalysts in 0.5 M H_2SO_4 solution. As shown in **Figure 3**a, linear sweep voltammograms (LSV) were carried out to evaluate the OER activity of these catalysts compared with the commercial RuO_2 reference. The polarization curves show that $RuNi_2$©G-250 catalyst exhibits the best activity with a lower overpotential of 227 mV at 10 mA cm^{-2}, significantly better than the commercial RuO_2 of 290 mV (Figure 3a and Figure S5, Supporting Information). Besides, $RuNi_2$©G-250 delivers a mass activity of 57.6 mA mg^{-1} and a specific activity of 1688.8 mA cm^{-2} mg_{Ru}^{-1} at an overpotential of 250 mV, which are 5.7 and 25 times larger than that of commercial RuO_2 (Figure S6a,b, Supporting Information).

The Tafel plots in Figure S6c (Supporting Information) present a much smaller slope of 65 mV dec^{-1} for $RuNi_2$©G-250 compared with the slope of 95 mV dec^{-1} for commercial RuO_2. Compared to the different catalysts with similar mass loadings, $RuNi_2$©G-250 catalyst exhibited high activity at the current density of 10 mA cm_{geo}^{-2} (Table S1, Supporting Information), making it a promising material for acidic oxygen evolution.

In addition, the oxidation temperature and feed molar ratio of Ru and Ni precursors have a significant effect on the OER activity. As shown in Figure 3b, the OER activity increases first and then decreases with the rise of oxidation temperature, in which $RuNi_2$©G-250 possesses the best activity. The reason may be that lower oxidation temperature can not destroy the graphene shell and thus unable to oxidize the inner core to form RuO_2. While the higher oxidation temperature over 250 °C leads to graphene shell decreased and even disappeared, which can not afford to form the unique interface between RuO_2 and graphene (insert in Figure 3b). To further prove the beneficial effect of interface between RuO_2 and graphene for $RuNi_2$©G-250 catalyst, we prepared a $RuNi_2O_x$ sample without graphene shell (Figure S7, Supporting Information) and RuO_2 physically mixed with graphene, and evaluated their OER activity. As shown in Figures S8 and S9 (Supporting Information), $RuNi_2$©G-250 delivers a better activity than the $RuNi_2O_x$ sample and RuO_2 physically mixed with graphene, which further reveals the significant role of interface Ru centers between RuO_2 and graphene. Besides, the feed molar ratio of Ru and Ni precursors greatly affects the OER activity (Figure S10, Supporting Information), in which the molar ratio of 1:2 delivers the best OER activity. It may because that the introduced Ni precursors facilitate the growth of graphene, affecting the construction of interface between RuO_2 and graphene. These results further validate the interface between RuO_2 and graphene is a key factor to promote the oxygen evolution activity in acidic electrolyte.

Besides the activity, the constant current chronopotentiometry was adopted to assess the durability of $RuNi_2$©G-250. In the case of commercial RuO_2 supported on glassy carbon, we found that it deactivated rapidly to a similar activity of the glassy carbon reference after around 0.3 h at a current density of 10 mA cm^{-2}, much inferior to the $RuNi_2$©G-250 at the same mass loading (Figure 3c). Further, $RuNi_2$©G-250 was supported on carbon fiber to increase the catalyst loading and decrease the effect of bubbles on the catalyst surface to assess its lifetime. It was found that the $RuNi_2$©G-250 catalyst can catalyze the acidic OER stably for more than 24 h at 10 mA cm^{-2} (Figure 3d). The post chronopotentiometry electrolyte analyzed by inductively coupled plasma optical emission spectroscopy (Table S3, Supporting Information) indicated the Ru dissolution percentage relative to the initial mass loading was almost 1.5%, indicating a low Ru loss during the acidic OER process. This further demonstrates the interface between RuO_2 and graphene benefits for the stabilization of RuO_2 during the acidic OER process. Furthermore, Ru K-edge, XPS spectra and XRD analysis indicate that the electronic structure and valence state of Ru in $RuNi_2$©G-250 sample after 24 h stability test almost has no change compared with the fresh catalyst (Figure 3e–f, and Figures S11,S12, Supporting Information). The unique interface between RuO_2 and graphene preserved well characterized by the HRTEM images in Figure S12 (Supporting Information). These results indicate that the unique interface between RuO_2 and graphene of the $RuNi_2$©G-250 efficiently promotes both activity and durability of OER in acidic electrolyte.

In order to gain further insights into the nature of $RuNi_2$©G-250 towards acidic OER, DFT calculations were employed to reveal the active sites and reaction mechanism. The graphene nanoflake coating on RuO_2 surface structure was constructed for modeling the catalyst with different sites toward OER (**Figure 4**a and Figure S13, Supporting Information). It is generally agreed that the adsorption energies of three intermediates HO*, O*, and HOO* involved in OER steps significantly influence the overpotential.[27–31] As shown in Figure 4b and Table S4 (Supporting Information), the free energies of HO* and O* are slightly stabilized at the interface Ru centers due to the non-covalent interaction such as van de Waals or electrostatic interaction. More importantly, however, the free energy of HOO* can be altered in a quite broad range. And the free energy of HOO* species can be stabilized more significantly than that of O* species after constructing the interface Ru centers between RuO_2 and graphene, which is independent of the different crystal planes of RuO_2 (Table S5, Supporting Information). Consequently, the classic scaling relationships between HOO* and HO* can be broken, leading to an optimization of the whole OER process. Compared to the other sites including the pristine RuO_2 site, above graphene site and Ru site under graphene etc., the interface Ru centers between RuO_2 and graphene with armchair edge presented the lowest overpotential, showing the best OER activity even better than the pristine RuO_2, which is in accordance with the experimental results (Figure 3a and 4b). Considering some nickel dopants may remain in the catalyst although nickel species leaching occurs inevitably under the OER acidic conditions (Figures S14,S15 and Table S3, Supporting Information), we also calculated the Ni-doping effect towards OER. As shown in Figure 4b and Table S4 (Supporting Information), the introduction of Ni into RuO_2 make no contribution on the improvement of OER activity. All in all, the interface Ru centers between RuO_2 and graphene with armchair edge is likely the active site. This result is coinciding with the experimental trend as shown in Figure 3b, where exists an optimal oxidation temperature to efficiently construct the interface between RuO_2 and graphene.

The free energy profiles were also calculated to investigate the nature of the activity difference between RuO_2 and $RuNi_2$©G-250. Figure 4c shows that the rate-determining step towards acidic OER for the interface Ru centers between RuO_2 and graphene is the conversion of HOO* to O_2, while for pristine RuO_2 is the conversion of O* to HOO*. In comparison with the limiting potential of 1.82 V for pristine RuO_2's rate-determining step, the interface Ru centers between RuO_2 and graphene possess a better activity with the significantly lower limiting potential of 1.64 V. This result implies that the interface Ru centers can efficiently reduce the limiting potential and enhance the acidic OER activity.

Furthermore, the differential charge density of the interface Ru centers between RuO_2 and graphene was adopted to rationalize the improved oxidation and corrosion resistance of $RuNi_2$©G-250 catalyst observed in the experiments. It is found that the RuO_2 gains a considerable amount of charge (1.2 e per cell) from the graphene (Figure 4d), which implies that the graphene could act as an electron reservoir to donate electrons to RuO_2 surface and

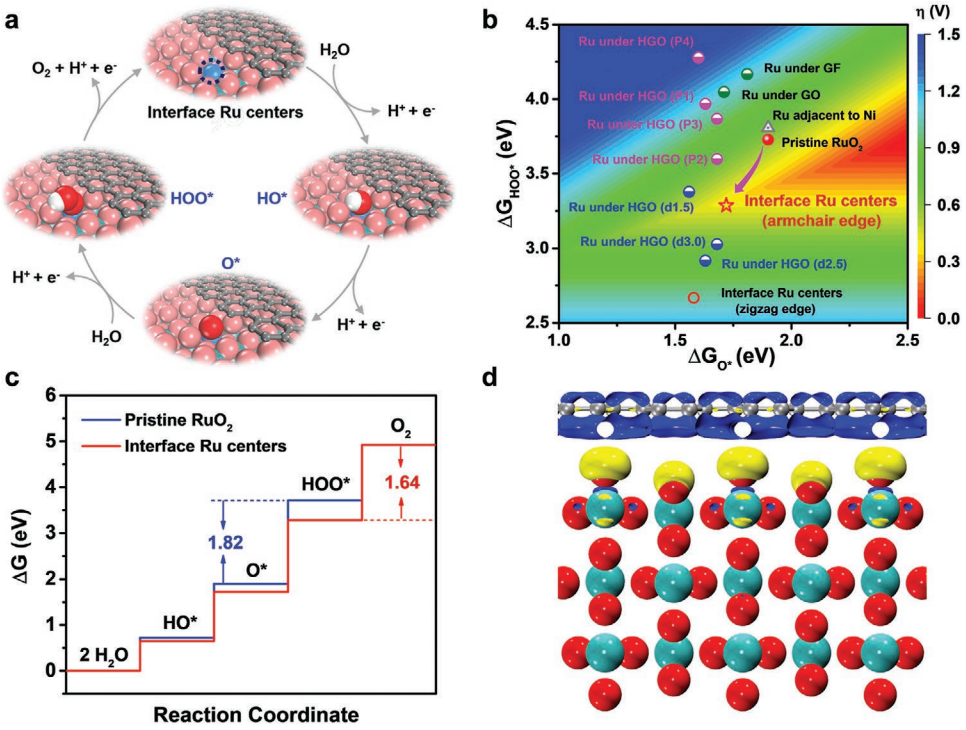

Figure 4. Theoretical interpretation of the activity and stability of OER over interface Ru centers between RuO_2 and graphene. a) The catalytical reaction circle and the active sites for interface Ru centers. The red, gray, white, and blue balls represent O, C, H, and Ru atoms, respectively. b) The calculated overpotential (η) against the free energy of O* (ΔG_{O^*}) and HOO* (ΔG_{HOO^*}) on different active sites: a pristine RuO_2 site, interface Ru centers, a Ru site under graphene or graphene oxide, and a Ru site adjacent to Ni (Ru adjacent to Ni); P1–P4 represent the graphene with different degrees of oxidation, and d1.5–d3.0 represent the different heights between graphene and RuO_2. c) Free energy profiles for the OER over RuO_2 and interface Ru centers between RuO_2 and graphene with armchair edge at zero potential ($U = 0$). d) Differential charge density at the interface Ru centers between RuO_2 and graphene. Yellow and blue contours represent electron accumulation and depletion, respectively. The isovalue is set to be 0.004 a.u.

thus enhance the resistance to over-oxidation and corrosion for RuO_2. Hence, the interface between RuO_2 and graphene not only efficiently boost the acidic OER activity, but also make an important contribution on the improvement of stability.

In summary, the interface Ru centers between RuO_2 and graphene were precisely constructed to enhance the electrocatalytic OER performance in an acidic electrolyte. The optimized catalyst $RuNi_2$@G-250 exhibited superior electrocatalytic activity compared with the commercial RuO_2, and a significant enhancement of lifetime exceeding 24 h durability test in 0.5 M H_2SO_4. Density functional theory calculations reveal that the interface Ru centers between RuO_2 and graphene can break the classic scaling relationships between the free energies of HOO* and HO* to reduce the limiting potential, rendering an enhancement in the intrinsic OER activity and resistance to over-oxidation and corrosion for RuO_2. The approach of constructing interface is general and may hold promise for other oxygen-evolution catalysts or, more broadly, to other reactions limited by intermediate adsorption-energy scaling relationships. These findings also pave an efficient way for rational design of electrocatalysts with highly catalytic activity and stability operated under harsh conditions.

Supporting Information

Supporting Information is available from the Wiley Online Library or from the author.

Acknowledgements

X.C. and P.R. contributed equally to this work. The authors gratefully acknowledge financial support from the National Key R&D Program of China (No. 2016YFA0204100 and 2016YFA0200200), the National Natural Science Foundation of China (No. 21890753, 21988101 and 21703274), the Key Research Program of Frontier Sciences of the Chinese Academy of Sciences (No. QYZDB-SSW-JSC020), and the DNL Cooperation Fund, Chinese Academy of Sciences (No. DNL180201 and DNL201918), the China Postdoctoral Science Foundation (No. 2018M642562), and the National Postdoctoral Program for Innovative Talents (BX201700140). We thank the staff at the BL14W1 beamline of the Shanghai Synchrotron Radiation Facilities for assistance with the XANES measurements.

Conflict of Interest

The authors declare no conflict of interest.

Keywords

acidic electrolytes, DFT calculations, electrocatalysis, interface active centers, oxygen evolution reaction

Received: December 10, 2019
Revised: March 26, 2020
Published online: May 17, 2020

[1] L. C. Seitz, C. F. Dickens, K. Nishio, Y. Hikita, J. Montoya, A. Doyle, C. Kirk, A. Vojvodic, H. Y. Hwang, J. K. Norskov, T. F. Jaramillo, *Science* **2016**, *353*, 1011.
[2] N. T. Suen, S. F. Hung, Q. Quan, N. Zhang, Y. J. Xu, H. M. Chen, *Chem. Soc. Rev.* **2017**, *46*, 337.
[3] F. S. Yu, D. Poole, S. Mathew, N. Yan, J. Hessels, N. Orth, I. Ivanovic-Burmazovic, J. N. H. Reek, *Angew. Chem., Int. Ed.* **2018**, *57*, 11247.
[4] Z. M. Chan, D. A. Kitchaev, J. N. Weker, C. Schnedermann, K. Lim, G. Ceder, W. Tumas, M. F. Toney, D. G. Nocera, *Proc. Natl. Acad. Sci. USA* **2018**, *115*, E5261.
[5] X. L. Zheng, B. Zhang, P. De Luna, Y. F. Liang, R. Comin, O. Voznyy, L. L. Han, F. P. G. de Arquer, M. Liu, C. T. Dinh, T. Regier, J. J. Dynes, S. S. He, H. L. L. Xin, H. S. Peng, D. Prendergast, X. W. Du, E. H. Sargent, *Nat. Chem.* **2018**, *10*, 149.
[6] N. Li, D. K. Bediako, R. G. Hadt, D. Hayes, T. J. Kempa, F. von Cube, D. C. Bell, L. X. Chen, D. G. Nocera, *Proc. Natl. Acad. Sci. USA* **2017**, *114*, 1486.
[7] Z. K. Goldsmith, A. K. Harshan, J. B. Gerken, M. Voros, G. Galli, S. S. Stahl, S. Hammes-Schiffer, *Proc. Natl. Acad. Sci. USA* **2017**, *114*, 3050.
[8] T. Reier, M. Oezaslan, P. Strasser, *ACS Catal.* **2012**, *2*, 1765.
[9] H. Q. Zhou, F. Yu, J. Y. Sun, R. He, S. Chen, C. W. Chu, Z. F. Ren, *Proc. Natl. Acad. Sci. USA* **2017**, *114*, 5607.
[10] K. A. Stoerzinger, O. Diaz-Morales, M. Kolb, R. R. Rao, R. Frydendal, L. Qiao, X. R. Wang, N. B. Halck, J. Rossmeisl, H. A. Hansen, T. Vegge, I. E. L. Stephens, M. T. M. Koper, Y. Shao-Horn, *ACS Energy Lett.* **2017**, *2*, 876.
[11] E. A. Paoli, F. Masini, R. Frydendal, D. Deiana, C. Schlaup, M. Malizia, T. W. Hansen, S. Horch, I. E. L. Stephens, I. Chorkendorff, *Chem. Sci.* **2015**, *6*, 190.
[12] Y. C. Yao, S. L. Hu, W. X. Chen, Z. Q. Huang, W. C. Wei, T. Yao, R. R. Liu, K. T. Zang, X. Q. Wang, G. Wu, W. J. Yuan, T. W. Yuan, B. Q. Zhu, W. Liu, Z. J. Li, D. S. He, Z. G. Xue, Y. Wang, X. S. Zheng, J. C. Dong, C. R. Chang, Y. X. Chen, X. Hong, J. Luo, S. Q. Wei, W. X. Li, P. Strasser, Y. E. Wu, Y. D. Li, *Nat. Catal.* **2019**, *2*, 304.
[13] R. H. Zhang, N. Dubouis, M. B. Osman, W. Yin, M. T. Sougrati, D. A. D. Corte, D. Giaume, A. Grimaud, *Angew. Chem., Int. Ed.* **2019**, *58*, 4571.
[14] D. Lebedev, Y. Pineda-Galvan, Y. Tokimaru, A. Fedorov, N. Kaeffer, C. Coperet, Y. Pushkar, *J. Am. Chem. Soc.* **2018**, *140*, 451.
[15] Z. W. Seh, J. Kibsgaard, C. F. Dickens, I. B. Chorkendorff, J. K. Norskov, T. F. Jaramillo, *Science* **2017**, *355*, eaad4998.
[16] L. Gloag, T. M. Benedetti, S. Cheong, Y. B. Li, X. H. Chan, L. M. Lacroix, S. L. Y. Chang, R. Arenal, I. Florea, H. Barron, A. S. Barnard, A. M. Henning, C. Zhao, W. Schuhmann, J. J. Gooding, R. D. Tilley, *Angew. Chem., Int. Ed.* **2018**, *57*, 10241.
[17] S. Laha, Y. Lee, F. Podjaski, D. Weber, V. Duppel, L. M. Schoop, F. Pielnhofer, C. Scheurer, K. Müller, U. Starke, K. Reuter, B. V. Lotsch, *Adv. Energy Mater.* **2019**, *9*, 1803795.
[18] T. Audichon, T. W. Napporn, C. Canaff, C. Morais, C. Comminges, K. B. Kokoh, *J. Phys. Chem. C* **2016**, *120*, 2562.
[19] J. Q. Shan, C. X. Guo, Y. H. Zhu, S. M. Chen, L. Song, M. Jaroniec, Y. Zheng, S. Z. Qiao, *Chem* **2019**, *5*, 445.
[20] H. N. Nong, T. Reier, H. S. Oh, M. Gliech, P. Paciok, T. H. T. Vu, D. Teschner, M. Heggen, V. Petkov, R. Schlögl, T. Jones, P. Strasser, *Nat. Catal.* **2018**, *1*, 841.
[21] A. Oh, H. Y. Kim, H. Baik, B. Kim, N. K. Chaudhari, S. H. Joo, K. Lee, *Adv. Mater.* **2019**, *31*, 1805546.
[22] J. W. Su, R. X. Ge, K. M. Jiang, Y. Dong, F. Hao, Z. Q. Tian, G. X. Chen, L. Chen, *Adv. Mater.* **2018**, *30*, 1801351.
[23] R. G. Gonzalez-Huerta, G. Ramos-Sanchez, P. B. Balbuena, *J. Power Sources* **2014**, *268*, 69.
[24] V. A. Saveleva, L. Wang, W. Luo, S. Zafeiratos, C. Ulhaq-Bouillet, A. S. Gago, K. A. Friedrich, E. R. Savinova, *J. Phys. Chem. Lett.* **2016**, *7*, 3240.
[25] J. Q. Shan, T. Ling, K. Davey, Y. Zheng, S. Z. Qiao, *Adv. Mater.* **2019**, *31*, 1900510.
[26] G. Wu, X. S. Zheng, P. X. Cui, H. Y. Jiang, X. Q. Wang, Y. T. Qu, W. X. Chen, Y. Lin, H. Li, X. Han, Y. M. Hu, P. G. Liu, Q. H. Zhang, J. J. Ge, Y. C. Yao, R. B. Sun, Y. E. Wu, L. Gu, X. Hong, Y. D. Li, *Nat. Commun.* **2019**, *10*, 4855.
[27] Y. Jiao, Y. Zheng, M. T. Jaroniec, S. Z. Qiao, *Chem. Soc. Rev.* **2015**, *44*, 2060.
[28] X. J. Cui, P. J. Ren, D. H. Deng, J. Deng, X. H. Bao, *Energy Environ. Sci.* **2016**, *9*, 123.
[29] R. R. Rao, M. J. Kolb, N. B. Halck, A. F. Pedersen, A. Mehta, H. You, K. A. Stoerzinger, Z. X. Feng, H. A. Hansen, H. Zhou, L. Giordano, J. Rossmeisl, T. Vegge, I. Chorkendorff, I. E. L. Stephens, Y. Shao-Horn, *Energy Environ. Sci.* **2017**, *10*, 2626.
[30] I. C. Man, H. Y. Su, F. Calle-Vallejo, H. A. Hansen, J. I. Martinez, N. G. Inoglu, J. Kitchin, T. F. Jaramillo, J. K. Norskov, J. Rossmeisl, *ChemCatChem* **2011**, *3*, 1159.
[31] A. D. Doyle, J. H. Montoya, A. Vojvodic, *ChemCatChem* **2015**, *7*, 738.
[32] L. Atanasoska, W. E. Ogrady, R. T. Atanasoski, F. H. Pollak, *Surf. Sci.* **1988**, *202*, 142.
[33] J. Y. Shen, A. Adnot, S. Kaliaguine, *Appl. Surf. Sci.* **1991**, *51*, 47.